scientific reports

Check for updates

OPEN

The capillary pressure vs. saturation curve for a fractured rock mass: fracture and matrix contributions

Alejandro Cardona [1,2], Qi Liu [2✉] & J. Carlos Santamarina [2,3]

The fractal topography of fracture surfaces challenges the upscaling of laboratory test results to the field scale, therefore the study of rock masses often requires numerical experimentation. We generate digital fracture analogues and model invasion percolation to investigate the capillarity-saturation P_c-S_w fracture response to changes in boundary conditions. Results show that aperture is Gaussian-distributed and the coefficient of variation is scale-independent. The aperture contraction during normal stress increments causes higher capillary pressures and steeper P_c-S_w curves, while shear displacement results in invasion anisotropy. The three-parameter van Genutchen model adequately fits the fracture capillary response in all cases; the capillary entry value decreases with fracture size, yet the fracture P_c-S_w curve normalized by the entry value is size-independent. Finally, we combine the fracture and matrix response to infer the rock mass response. Fracture spacing, aperture statistics and matrix porosity determine the rock mass capillarity-saturation P_c-S_w curve. Fractures without gouge control the entry pressure whereas the matrix regulates the residual saturation at high capillary pressure P_c.

List of symbols

a_i [m]	Sinusoid amplitude
A_c [m²]	True contact fracture area
A_f [m²]	Apparent fracture area
C	Fourier transform scaling factor
d [m]	Fracture spacing
f	Probability density function (sub-z_i: sinusoid; sub-z: sum of the sinusoids; sub-h: aperture)
G [m³]	Power spectral density
h [m]	Fracture aperture (sub-avg: average)
L [m]	Fracture size (sub-x: x-direction; sub-y: y-direction)
m	Fitting parameters in the van Genutchen model (sub-1: first parameter; sub-2: second parameter)
n	Matrix porosity
N	Aperture field size
N_p	Lattice size for invasion percolation model
P_0 [Pa]	Fitting parameter in the van Genutchen model
P_c [Pa]	Capillary pressure
r [m]	Matrix pore size
s [m]	Standard deviation (sub-h: aperture; sub-z: surface topography; sub-zt: top surface, sub-zb: bottom surface)
S_w	Wetting phase saturation (sup-RM: rock mass)
T_s [N/m]	Interfacial tension
V_v [m³]	Void volume (sup-F: fracture; sup-M: matrix)
$X(\lambda)$ [m]	Asperity amplitude for a given wavelength
z [m]	Surface topography (sub-t: top surface; sub-b: bottom surface)

[1]Institute for Geophysics, Jackson School of Geosciences, The University of Texas at Austin, 10601 Exploration Way, Austin, TX 78758, USA. [2]King Abdullah University of Science and Technology KAUST, Thuwal 23955-6900, Saudi Arabia. [3]School of Civil and Environmental Engineering, Georgia Institute of Technology, 790 Atlantic Drive, N.W., Atlanta, GA 30332, USA. ✉email: qi.liu@kaust.edu.sa

nature portfolio

1

α [m^3]	Spectral density at $\lambda = 1$ m
β	Power spectral density sensitivity to wavelength
δ [m]	Fracture displacement (sub-v: vertical; sub-x: x-direction)
Δl [m]	Cell size for invasion percolation model
Δx [m]	Sampling interval for fracture generation
η	Void fraction (sup-F: fracture; sup-M: matrix)
θ [deg]	Contact angle
λ [m]	Asperity wavelength (sub-max: maximum)
μ [m]	Mean (sub-h: aperture; sub-z: surface topography; sub-zt: top surface, sub-zb: bottom surface)
σ [Pa]	Normal stress
σ_y [Pa]	Material yield stress
φ_i [m]	Sinusoid phase
ω_i [m]	Sinusoid frequency

Mixed fluid conditions are common in fractured rocks and affect both engineering applications and natural processes[1,2]. Examples include energy resource extraction such as hydrocarbons and geothermal[3,4], the vadose zone and environmental remediation[5,6], geological storage of CO_2 and nuclear waste[7,8], and hydrothermal alteration and ore deposition[9].

In the absence of gouge, fractures provide preferential flow pathways that dominate fluid flow. Then, invasion can readily bypass wetting (and even non-wetting) fluids in the matrix and fast injection studies tend to conclude low displacement efficiency (e.g., CO_2 injection due to viscous fingering, and aggravated by fractures and heterogeneity). On the other hand, long-term analyses must be based on capillarity-saturation curves at thermodynamic equilibrium.

Pore size distribution, pore interconnectivity and spatial variability determine the relationship between the capillary pressure and the degree of saturation at equilibrium P_c-S_w[10]. These constitutive equations capture the entry pressure and the sensitivity of saturation to changes in capillary pressure. Most numerical codes rely on these expressions to analyze coupled processes[11,12].

Measurement techniques for the intact rock *matrix* are well established and rely on porous plates and tensiometers[13], mercury injection[14], centrifuge methods[15], controlled suction[16,17], dew point hydrometer[18], and thermal/electrical conductivity measurements on calibrated porous stones[19]. The measured capillary pressure–saturation curves are relatively smooth for intact rocks and can be fitted with simple functions[20,21].

In general, we can anticipate that the geometric aperture and its spatial correlation control capillary phenomena in *fractures*[22,23]. However, stress-sensitive aperture[24–26], fractal fracture topography[27], specimen size limitations and fracture-matrix interaction hinder the experimental determination of P_c-S_w curves in fractures and fractured rocks[28–30]. Furthermore, P_c-S_w curves would take weeks to months to reach thermodynamic equilibrium, particularly when trapped zones equilibrate through dissolution-diffusion processes[31,32]; in fact, most published laboratory studies report rapid fluid invasion tests[33].

In view of spatial and temporal scale limitations, numerical experimentation emerges as a necessary tool to study mixed fluid conditions in fractured rocks under long-term thermodynamic equilibrium. Previous numerical studies have explored the link between the fracture aperture and capillary pressure[34–36], and their associated changes with normal stress[37,38]. Yet, realistic fracture surface generation algorithms, the evolution of aperture with normal stress and shear displacement, and implications on the capillarity of fractured rock masses require further research.

This study explores the relationship between capillary pressure and saturation in fractured rocks, with emphasis on fracture-matrix interaction *at equilibrium* following the invasion of a non-wetting phase (Note: fast immiscible fluid invasion and transient saturation are not part of this study).

Fracture studies: methodology

First, we investigate the effects of normal stress, shear displacement and fracture surface topography on the fracture capillary response. We generate digital fracture analogues that resemble natural fractures and bring the two rough surfaces together to create the fracture pore space. Then, we use network model simulations to investigate the effects of surface roughness and matedness on the fracture capillarity-saturation curve, and its evolution during normal loading and shear displacement. Fracture generation, response to normal stress and shear displacement, and fluid invasion modeling are described next.

Fracture generation. The power spectral density of rock fracture surfaces $G(\lambda)$ [m^3] follows a power law with respect to wavelength λ [m][27,39,40] (Fig. 1a):

$$G(\lambda) = \alpha \left(\frac{\lambda}{\lambda_{ref}} \right)^{\beta}, \tag{1}$$

where the reference wavelength is $\lambda_{ref} = 1$m. This power equation implies a fractal topography and provides a convenient framework for numerical studies. The wave amplitude $X(\lambda)$ [m] for a certain wavelength λ is related to the spectral density as $G(\lambda) = C |X(\lambda)|^2$, where the scaling factor $C = N\Delta x/4$ [m] depends on the selected Fourier pair and transform definition (i.e., one-sided vs. two-sided). We use the Inverse Fast Fourier Transform to synthesize the surface roughness profile in space by assuming a uniformly distributed random phase (see similar surface generation models in Refs.[38,41]). The fractal topography implies lack of a characteristic scale or
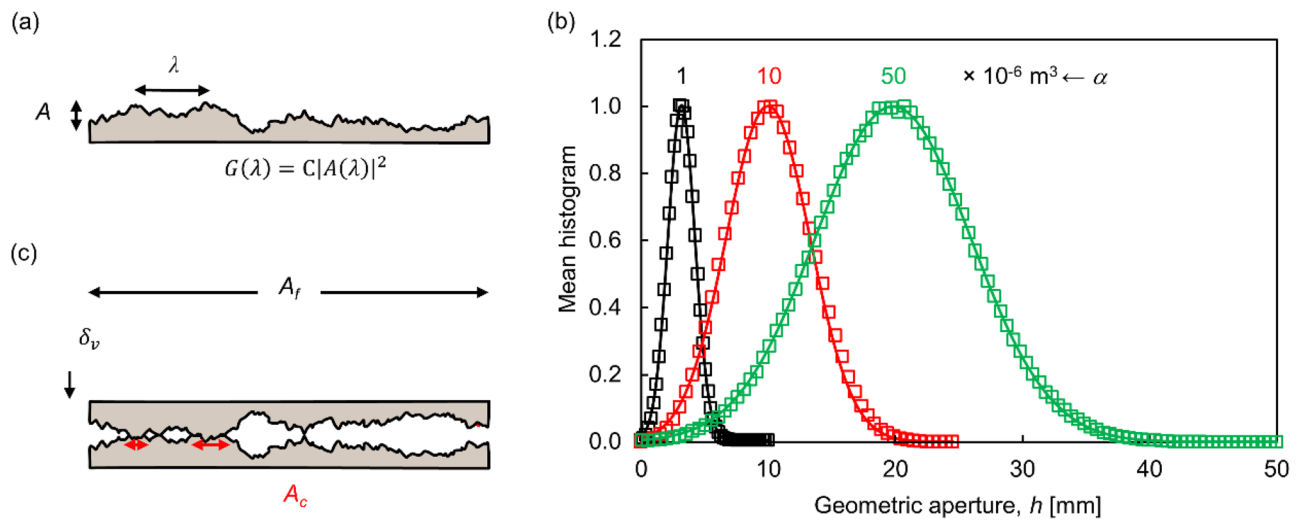
Figure 1. Fracture generation and deformation model. (**a**) Surface roughness ($\alpha = 1 \times 10^{-6}$ m^3, $\beta = 2.9$. Vertical cross-section of a 3D fracture; scale exaggerated by a factor of $\sim$2). (**b**) Geometric aperture distribution for "unmated" 3D fracture surfaces. Mean trends based on 100 realizations (markers: computed values; solid lines: fitted normal distribution). Black: $\alpha = 1 \times 10^{-6}$ m^3, $\beta = 2.9$, $\mu_h = 3.2$ mm, $s_h = 1$ mm; red: $\beta = 2.9$, $\alpha = 1 \times 10^{-5}$ m^3, $\mu_h = 10$ mm, $s_h = 3.3$ mm; green: $\alpha = 5 \times 10^{-5}$ m^3, $\beta = 2.9$, $\mu_h = 19.8$ mm, $s_h = 6$ mm. Fracture size: 0.1 × 0.1 m, cell size: 0.1 mm. (**c**) Contact model: $A_c = A_f (\sigma / \sigma_y)$.

representative equivalent size. However, fractal geometries have limits in natural systems; in our case, the longest wavelength is the fracture size under consideration.

Two contiguous rock surfaces define a fracture. We capture matedness by considering the correlation between them. There are two end-members: "perfectly mated fractures" consist of two identical surfaces with opposite orientations, and "unmated fractures" which are made of two uncorrelated surfaces. Figure 1b shows the aperture size distribution of unmated fracture surfaces generated using various α-factors (Eq. (1)).

Fracture deformation. *Deformation due to normal stress.* We adopt a simple rigid-plastic contact model to compute the normal deformation due to a normal stress σ [MPa]. The rock reaches its yield stress σ_y [MPa] at the true fracture contact area A_c [m^2]. Then, equilibrium implies,

$$A_c(\sigma) = A_f \frac{\sigma}{\sigma_y}, \tag{2}$$

where A_f [m^2] is the total fracture area. The two fracture surfaces interpenetrate a vertical distance δ_v to satisfy the computed contact area A_c (Eq. (2)—see Fig. 1c). While mass is not conserved at contacts, its effect on aperture distribution is negligible due to the small contact area A_c. The selected rigid-plastic model depends on a single variable -the yield stress σ_y- in line with Ockham's principle of parsimony[42]. For comparison, the simplest elastoplastic model with post-peak softening requires ≥ 4 variables[38,43] and additional parameters would be needed to track the evolution of the yield strength with contact deformation[44]. The rigid-plastic model is simple to implement, supports robust analyses and is adequate for capillary studies.

Shear displacement. We impose shear by displacing the two surfaces as rigid bodies without changing their surface topographies; natural processes are more complex and involve asperity shearing and/or overriding. The periodic boundary condition maintains a constant fracture area A_f during shear displacement whereby the moving surface re-appears on the opposite side. This boundary condition assumes the shear displacement is a subset of an infinite medium.

Invasion percolation for drainage. After shear displacement and normal loading, we map the resulting $N \times N$ aperture field $h_{i,j}$ with spatial resolution $\Delta x = \Delta y$ onto a $N_p \times N_p$ square lattice with fourfold connectivity where $N_p < N$ (i.e., a "checkerboard" model—see Refs.[45–47]). The height h_{avg} of each cell is the average aperture in the original fracture within the corresponding area $\Delta l \times \Delta l$, so that $\sum h_{i,j} \Delta x^2 \approx h_{avg} \Delta l^2$.

The selected cell size $\Delta l \times \Delta l$ defines the aperture resolution. While the pressure-dependent saturation of a given pore depends on the pore geometry, the global trends exhibit limited sensitivity to local details: results from a focused numerical study reveal that aperture averaging in $\Delta l \times \Delta l$ affects only the lower end of the capillary-saturation P_c-S_w curve, i.e., at high capillary pressures and low degrees of saturation. Furthermore, apertures h are much smaller than wavelengths in natural fractures ($h/\lambda << 1$—Ref.[27]); therefore, the in-plane radius of curvature is negligible and capillarity-saturation results are unaffected by aperture averaging when $\Delta l < 10\Delta x$. Previous studies show that the in-plane curvature can influence invasion patterns[34,38,48]; however, our fracture generation model ensures $h/\lambda << 1$ and the capillary pressure is only a function of the aperture.

The invasion percolation algorithm assumes equilibrium at any given pressure (i.e., neither viscous forces nor time effects), and non-trapping of the wetting phase. Various pore-scale phenomena justify the non-trapping assumption, including (Fig. 2): corner flow along rough surfaces[31], fluid transport into the matrix[49,50], water evaporation and vapor pressure equilibration[51]. While these processes have characteristic time scales, the equilibrium assumption disregards any transient trapping of the wetting phase.

We implement the Young–Laplace equation in terms of the aperture-induced curvature, $P_c = T_s/h$ (Note: this expression assumes cylindrical interfaces given that $h < \Delta l$ and a perfectly wetting mineral surface $\theta = 0°$). The largest aperture connected to the inlet is invaded first and defines the entry value. All apertures connected to the non-wetting phase throughout the medium are candidates for invasion. Invasion proceeds by monotonically increasing the capillary pressure to define the capillary pressure versus saturation P_c-S_w curve.

Results

The fracture P_c-S_w curve.
Fractures vary over a wide range of length scales. Figure 3 shows the aperture size distribution for three uncorrelated and unmated fractures of size $L_x \times L_y = 1 \times 1$ m, 0.1×0.1 m and 0.01×0.01 m subjected to zero normal stress (power spectral density parameters: $\alpha = 1 \times 10^{-6}$ m³, $\beta = 2.9$). The selected fracture variables represent natural conditions and highlight size effects. Each curve represents an average of 100 numerical realizations in order to obtain statistically representative results. The mean aperture size distribution
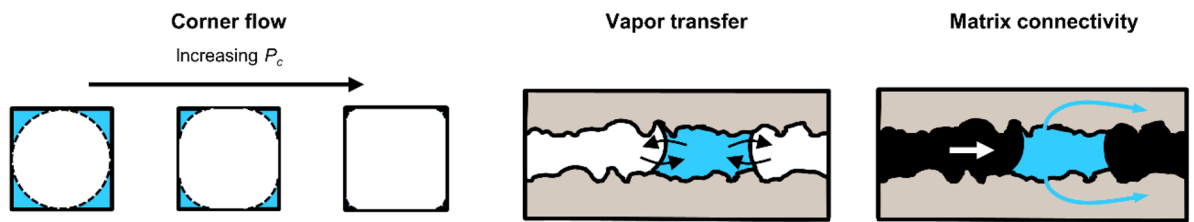

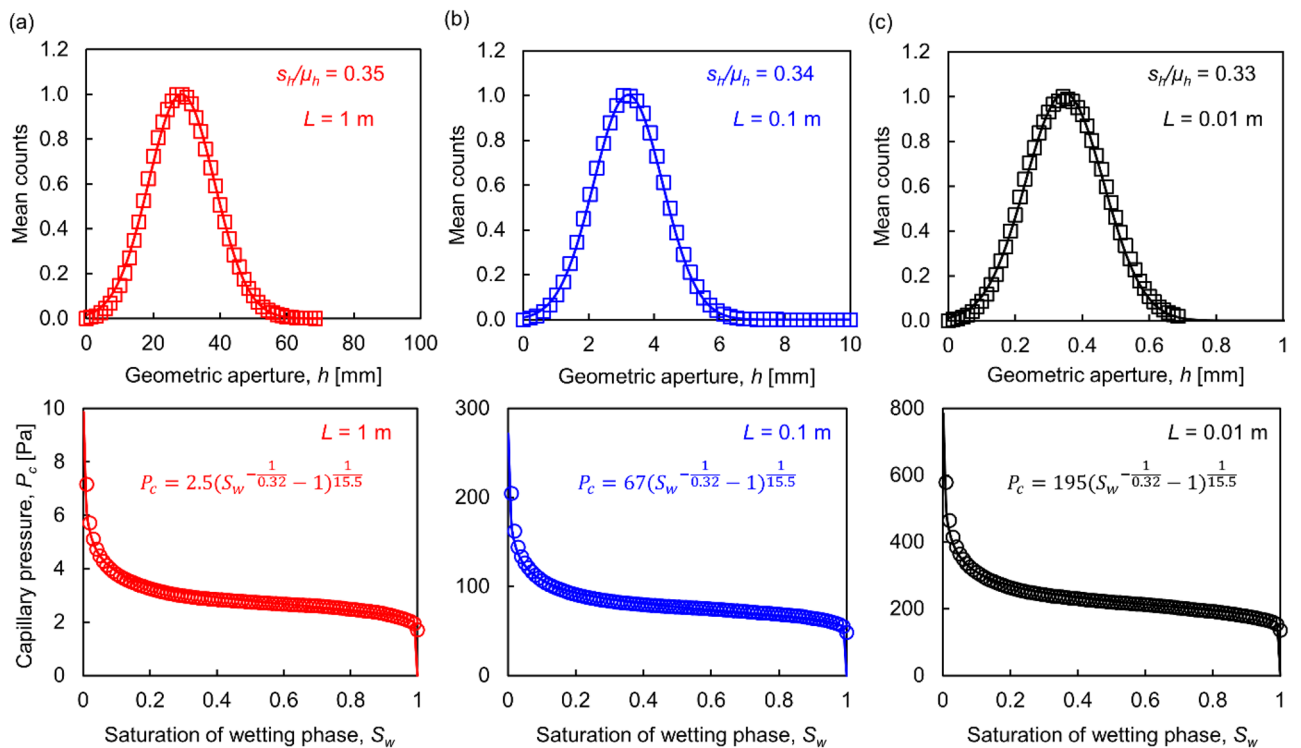**Figure 2.** Processes involved in preventing the trapping of the wetting phase in fractures.

Figure 3. Aperture size distribution and P_c-S_w curves for uncorrelated fractures of size LxL. (**a**) $L = 1$ m. (**b**) $L = 0.1$ m. (**c**) $L = 0.01$ m. The number of cells is $N_p \times N_p = 100 \times 100$ in all cases, therefore, the cell size Δl decreases proportionally to fracture size. Unmated fractures generated with power spectral density parameters $\alpha = 1 \times 10^{-6}$ m³ and $\beta = 2.9$ (Eq. (1)). Numerical results shown as empty markers are the mean values of 100 numerical realizations and are fitted with a Gaussian distribution (geometric aperture) and the van Genuchten model (capillary pressure).

is Gaussian-distributed in the three cases, with almost the same coefficient of variation s_h/μ_h defined in terms of the aperture standard deviation s_h and the mean aperture μ_h (see Fig. 3).

The capillary pressure P_c at a given saturation S_w increases as the fracture size decreases due to inverse relationship between aperture and fracture size. We fit the mean P_c-S_w curve using the three-parameter van Genutchen model[52]:

$$P_c = P_0\left(S_w^{-1/m_1} - 1\right)^{1/m_2}, \tag{3}$$

where P_0 [Pa] relates to the entry value, and m_1 and m_2 capture the sensitivity of saturation to capillary pressure. This three-parameter model provides an excellent fit compared to the two-parameter van Genutchen and Brooks-Corey models. While the P_0 value is inversely proportional to the fracture size L, the m_1 and m_2 parameters remain constant regardless of the fracture size for surfaces generated with the same power spectral density α and β parameters (Eq. (1)); hence, the normalized $(P_c/P_0) - S_w$ curves are scale-independent.

The effect of normal stress. As the normal stress increases, the aperture size distribution shifts towards smaller values and a cutoff at zero aperture emerges as contact yield results in zero aperture contact points (Fig. 4a). The coefficient of variation of the fitted truncated Gaussian distributions increases with normal stress, and the aperture field exhibits higher variability.

Reduced apertures require higher capillary pressures for the same degree of saturation and the slope of the P_c-S_w curve increases (Fig. 4b). The evolution of the van Genutchen model parameters P_0, m_1 and m_2 are shown in the inset (Fig. 4b). Note that higher normal stress and fracture closure increase the degree of saturation of the wetting phase at constant capillary pressure (see arrow in Fig. 4b).

The effect of shear displacement. The shearing of unmated, uncorrelated fracture surfaces results in statistically identical aperture fields and the capillarity-saturation P_c-S_w trends remain the same (in the absence of asperity shearing and gouge formation).

Shear displacement causes aperture changes only when there is some initial degree of matedness between surfaces[27]. Figure 5 shows the capillarity-saturation P_c-S_w curves for initially mated fractures: as the shear displacement increases, the mean aperture increases and the capillary pressure decreases for a given degree of saturation.

Shear displacement induces anisotropy in the aperture field of initially mated fractures as aperture ridges emerge transverse to the shear direction. Results in Fig. 5 show that the ensuing anisotropy in aperture
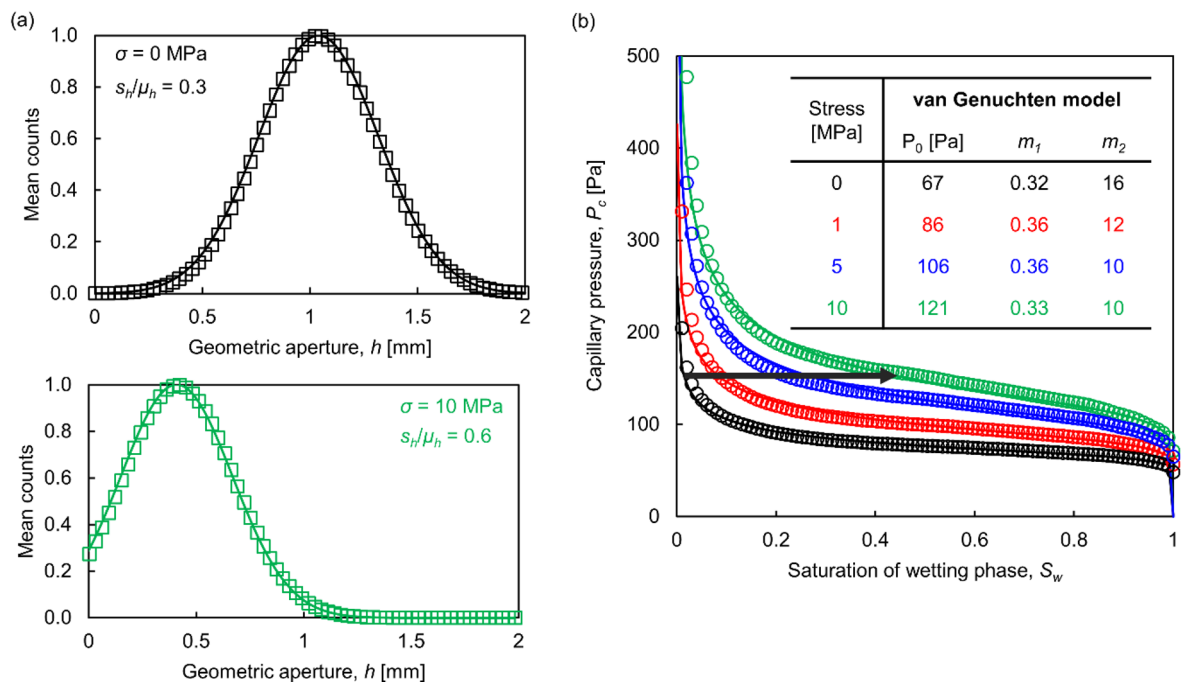

Figure 4. Evolution of fracture aperture and P_c-S_w curve with normal stress. (**a**) Aperture size distribution at normal stress $\sigma = 0$ and $\sigma = 10$ MPa. Numerical results shown as empty markers are the mean values of 100 numerical realizations and are fitted with truncated Gaussian distribution (model parameters: $\alpha = 1 \times 10^{-7}$ m^3, $\beta = 2.9$, $L \times L = 0.1 \times 0.1$ m, $\Delta l = 1$ mm, $\sigma_y = 200$ MPa). (**b**) P_c-S_w curve for unmated fractures subjected to normal stress. The van Genuchten model (solid line) is used to fit numerical results (empty markers: mean of 100 numerical realizations). The arrow indicates the saturation path for a fracture that experiences an increase in normal stress at constant capillary pressure.
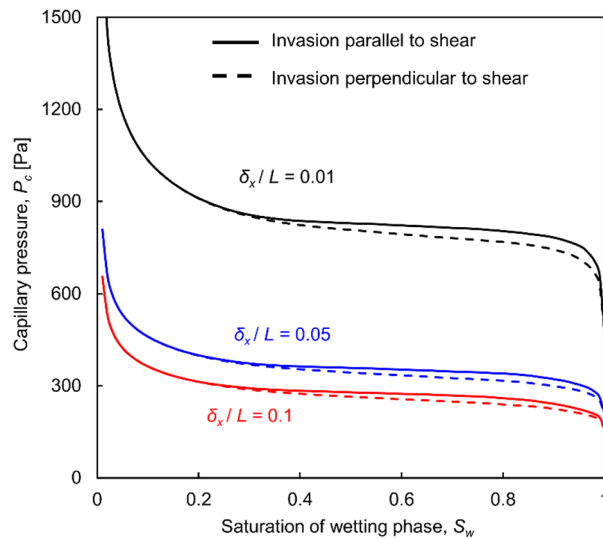
Figure 5. Capillary pressure vs. saturation P_c-S_w curves for initially mated fractures that experience shear displacement at zero normal stress. Shear displacement occurs along the x-direction and is normalized with respect to the fracture sizes L. Plotted results are the mean values of 100 realizations. Model parameters: $\alpha = 1 \times 10^{-6}$ m³, $\beta = 2.9$, $L \times L = 0.01 \times 0.01$ m, $\Delta l = 0.1$ mm.

connectivity produces slightly different P_c-S_w curves -particularly at low P_c values- when the capillary pressure is controlled at a boundary that is normal or parallel to ridges.

The P_c-S_w curve for the fractured rock mass. The fracture and matrix P_c-S_w curves combine to define the capillary response of the fractured rock mass. Consider three orthogonal fracture sets with the same spacing d in the three directions so that the repetitive unit is of size d^3 (Fig. 6a). The matrix porosity n, the mean aperture size μ_h and the fracture spacing d determine the volume of voids in the matrix $V_v^M \approx nd^3$ and in fractures $V_v^F \approx 3d^3(\mu_h/d)$ for $\mu_h/d \ll 1$. The volume of voids in the matrix V_v^M becomes a significant fraction of the total volume of voids $V_v^M + V_v^F$ for small aperture to spacing ratios μ_h/d and high matrix porosity n:

$$\eta^M = \frac{V_v^M}{V_v^M + V_v^F} \approx \frac{n}{n + 3\left(\frac{\mu_h}{d}\right)}. \tag{4}$$

Conversely, the storativity in fractures gains relevance in rock masses with low matrix porosity n

$$\eta^F = \frac{V_v^F}{V_v^M + V_v^F} \approx \frac{3\left(\frac{\mu_h}{d}\right)}{n + 3\left(\frac{\mu_h}{d}\right)}, \tag{5}$$

where $\eta^F = 1 - \eta^M$. The fracture and the matrix share the same capillary pressure at equilibrium, therefore, the resultant $P_c - S_w$ curve is a void-volume average of the saturation contributed by the fracture and the matrix $S_w^{RM} = S_w^F(1 - \eta^M) + S_w^M \eta^M$.

Let's consider the matrix and the fracture P_c-S_w curves and combine them for various matrix void fractions η^M to estimate the rock mass capillary response. We compute the fracture P_c-S_w curve using the algorithm described above, and a similar algorithm for the matrix where pores are represented as connected tubes with capillary pressure $P_c = 2T_s/r$ (see model details in Ref.[53]). Results in Fig. 6 show that fractures -without gouge- control the entry pressure, whereas the matrix dominates the behavior at high capillary pressure. As the η^M fraction increases, the rock mass capillary-saturation curves approach the matrix P_c-S_w curve.

Discussion

The long-term saturation of a fractured rock mass will depend on the capillary pressure and the degree of saturation at equilibrium P_c-S_w. This will determine the original oil saturation profile in the reservoir and the residual oil after production, the long-term CO_2 and H_2 storage capacity, the distribution of LNAPLs and DNAPLs contaminants and environmental remediation strategies, the residual distribution of hydraulic fracturing fluids and the relative permeability of the resulting fractured rock mass.

The numerical study revealed surprising emergent properties. In particular, why is the aperture coefficient of variation s_h/μ_h independent of fracture size? (Fig. 3). The fracture surface topography z is the sum of k independent sinusoids with amplitudes a_i that follow the power law in Eq. (1) and random phase φ_i, $z = \sum_j^k z_j = \sum_i a_i \sin(\omega_i x_j + \varphi_i)$. The probability density function of the sum of random variables f_z is the convolution of the individual density functions, $f_z = f_{z_1} * f_{z_2} \ldots * f_{z_k}$. In the limit $k \to \infty$, the central limit theorem emerges and f_z converges to a Gaussian distribution[54]. While the central limit theorem often requires f_{z_i} to be
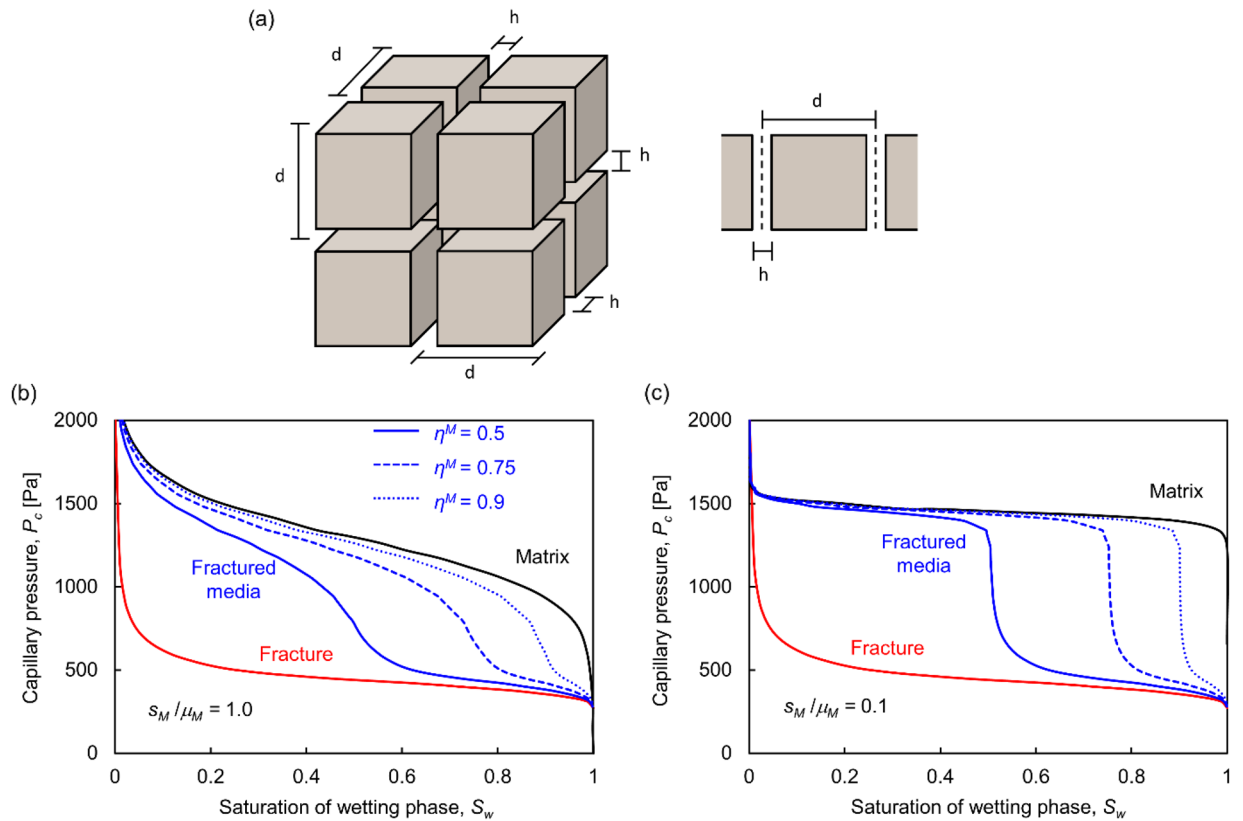
Figure 6. Fractured rock mass capillary behavior. (**a**) The fractured rock mass with three orthogonal fracture sets with the same spacing d in the three directions. (**b,c**) P_c-S_w curve for the fractured medium with a (**b**) heterogeneous ($s_M/\mu_M = 1.0$) and (**c**) homogeneous ($s_M/\mu_M = 0.1$) rock matrix lognormal pore size distribution (see Ref.[53] for rock matrix pore network model). Model parameters used to compute the fracture P_c-S_w curve: $\alpha = 1 \times 10^{-7}$ m³, $\beta = 2.9$, $L \times L = 0.1 \times 0.1$ m, $\Delta l = 1$ mm. Model parameters for the matrix: $\mu_M = 0.1$ mm, $L \times L = 0.1 \times 0.1$ m, $\Delta l = 1$ mm.

independent and identically distributed, f_z can converge to a Gaussian distribution for non-identical density functions (Lyapunov's Central limit theorem—Ref.[55]). Then, the fracture surface topography z satisfies a Gaussian distribution, $z \sim N(\mu_z, s_z^2)$.

The fracture geometric aperture is the subtraction of the top z_t and bottom z_b surface topographies, $h = z_t - z_b$. Therefore, the fracture aperture values also exhibit a Gaussian distribution when the two surfaces are uncorrelated $h \sim N(\mu_{zt} - \mu_{zb}, s_{zt}^2 + s_{zb}^2)$. The scale invariant features in our numerically generated fractures result from the fractal nature of the surface roughness[56].

The aperture Gaussian distribution f_h allows us to obtain the lower bound of the P_c-S_w curve: the pore volume distribution is $f_v = (h \times \Delta l^2) f_h$, then, the cumulative distribution function of f_v (from largest to smallest h) normalized by the integral of $(h \times \Delta l^2)$ corresponds to the wetting phase saturation S_w with capillary pressure $P_c = T_s/h$.

Conclusions

The capillarity pressure vs. saturation response of fractured rock masses is needed for long-term analyses. However, the time needed to reach thermodynamic equilibrium and size-dependent fracture topology limit our ability to experimentally gather relevant capillarity-saturation curves.

Numerical experiments show that the capillary pressure versus saturation P_c-S_w curve for a fractured rock mass is determined by pore-scale characteristics in the fractures and the matrix, including aperture and pore size statistics, spatial variability and connectivity.

The fracture surface roughness can be synthesized as a sum of independent sinusoids. A power law relates the sinusoidal amplitudes to their wave wavelength. The central limit theory emerges and the aperture size follows a Gaussian distribution. The mean aperture increases with fracture-size, yet, the coefficient of variation s_h/μ_h is scale independent.

While the wetting phase could remain occluded in the matrix during non-wetting fluid invasion, trapping in fractures is limited. Wetting fluid connectivity allows for the wetting fluid to escape through a network of connected corners formed by the surface roughness or via the permeable porous matrix. Long-term equilibrium in liquid–vapor systems further promotes non-trapping conditions in fractures.

The increase in normal stress contracts the aperture and results in higher capillary pressure, increased aperture variability, increased true contact area and steeper P_c-S_w curves. Capillary invasion reflects a slight anisotropy

during shear and affects saturation at low capillary pressures. The three-parameter van Genutchen model captures the fracture P_c-S_w response and its evolution with normal stress and shear displacement. While the capillary entry value is inversely proportional to the fracture size, the normalized capillarity-saturation curves $(P_c/P_0) - S_w$ follow similar trends and are scale independent.

At equilibrium, fracture spacing and aperture statistics combine with the matrix porosity to determine the capillary pressure versus saturation curve for a rock mass and its storativity. In the absence of gouge, the fracture P_c-S_w curve controls the entry pressure, whereas the matrix regulates the rock mass residual saturation at high capillary pressures.

Data availability

The datasets used and/or analyzed during the current study are available from the corresponding author.

References

1. National Academies of Sciences, Engineering and Medicine. *Characterization, Modeling, Monitoring, and Remediation of Fractured Rock* (The National Academies Press, 2020). https://doi.org/10.17226/21742.
2. Berkowitz, B. Characterizing flow and transport in fractured geological media: A review. *Adv. Water Resour.* **25**, 861–884. https://doi.org/10.1016/S0309-1708(02)00042-8 (2002).
3. Blunt, M. J. *et al.* Pore-scale imaging and modelling. *Adv. Water Resour.* **51**, 197–216. https://doi.org/10.1016/j.advwatres.2012.03.003 (2013).
4. White, D., Muffler, L. & Truesdell, A. Vapor-dominated hydrothermal systems compared with hot-water systems. *Econ. Geol.* **66**, 75–97. https://doi.org/10.2113/gsecongeo.66.1.75 (1971).
5. Fredlund, D. G. The 1999 RM Hardy Lecture: The implementation of unsaturated soil mechanics into geotechnical engineering. *Can. Geotech. J.* **37**, 963–986. https://doi.org/10.1139/t00-026 (2000).
6. Gerke, H. H. & van Genuchten, M. T. A dual-porosity model for simulating the preferential movement of water and solutes in structured porous media. *Water Resour. Res.* **29**, 305–319. https://doi.org/10.1029/92WR02339 (1993).
7. Pruess, K. Enhanced geothermal systems (EGS) using CO2 as working fluid-A novel approach for generating renewable energy with simultaneous sequestration of carbon. *Geothermics* **35**, 351–367. https://doi.org/10.1016/j.geothermics.2006.08.002 (2006).
8. Gens, A. *et al.* A full-scale in situ heating test for high-level nuclear waste disposal: Observations, analysis and interpretation. *Géotechnique* **59**, 377–399. https://doi.org/10.1680/geot.2009.59.4.377 (2009).
9. Taylor, H. The application of oxygen and hydrogen isotope studies to problems of hydrothermal alteration and ore deposition. *Econ. Geol.* **69**, 843–883. https://doi.org/10.2113/gsecongeo.69.6.843 (1974).
10. Lu, N. & Likos, W. J. *Unsaturated Soil Mechanics* (Wiley, 2004).
11. Olivella, S., Carrera, J., Gens, A. & Alonso, E. E. Nonisothermal multiphase flow of brine and gas through saline media. *Transp. Porous Media* **15**, 271–293. https://doi.org/10.1007/BF00613282 (1994).
12. Liu, H.-H. & Bodvarsson, G. S. Constitutive relations for unsaturated flow in a fracture network. *J. Hydrol.* **252**, 116–125. https://doi.org/10.1016/S0022-1694(01)00449-8 (2001).
13. Pentland, C. H., El-Maghraby, R., Iglauer, S. & Blunt, M. J. Measurements of the capillary trapping of super-critical carbon dioxide in Berea sandstone. *Geophys. Res. Lett.* https://doi.org/10.1029/2011GL046683 (2011).
14. Purcell, W. R. Capillary pressures-their measurement using mercury and the calculation of permeability therefrom. *J. Petrol. Technol.* **1**, 39–48. https://doi.org/10.2118/949039-G (1949).
15. Slobod, R., Chambers, A. & Prehn, W. Jr. Use of centrifuge for determining connate water, residual oil, and capillary pressure curves of small core samples. *J. Petrol. Technol.* **3**, 127–134. https://doi.org/10.2118/951127-G (1951).
16. Romero, E., Lloret, A. & Gens, A. Development of a new suction and temperature controlled oedometer cell. In *1st International Conference on Unsaturated Soils* Vol 2 (eds Alonso, E. E. & Delage, P.)553–559 (A.A. Balkema, 1995).
17. Tarantino, A. *et al.* Benchmark of experimental techniques for measuring and controlling suction. *Géotechnique* **61**, 303–312. https://doi.org/10.1680/geot.2011.61.4.303 (2011).
18. Campbell, G. S., Smith, D. M. & Teare, B. L. Application of a dew point method to obtain the soil water characteristic. In *Experimental Unsaturated Soil Mechanics. Springer Proceedings in Physics* Vol. 112 (ed. Schanz, T.) https://doi.org/10.1007/3-540-69873-6_7 (Springer, Berlin, Heidelberg, 2007).
19. Richards, B. G. Behaviour of unsaturated soils. In *Soil Mechanics-New Horizons* (ed. Lee, I. K.) 112–157 (American Elsevier, 1974).
20. Brooks, R. H. & Corey, A. T. Hydraulic properties of porous media. *Hydrology Papers 3 (Colorado State University)* (1964).
21. van Genuchten, M. T. A closed-form equation for predicting the hydraulic conductivity of unsaturated soils. *Soil Sci. Soc. Am. J.* **44**, 892–898. https://doi.org/10.2136/sssaj1980.03615995004400050002x (1980).
22. Persoff, P. & Pruess, K. Two-phase flow visualization and relative permeability measurement in natural rough-walled rock fractures. *Water Resour. Res.* **31**, 1175–1186. https://doi.org/10.1029/95WR00171 (1995).
23. Pruess, K. & Tsang, Y. W. On two-phase relative permeability and capillary pressure of rough-walled rock fractures. *Water Resour. Res.* **26**, 1915–1926. https://doi.org/10.1029/WR026i009p01915 (1990).
24. Haghi, A. H. & Chalaturnyk, R. Experimental characterization of hydrodynamic properties of a deformable rock fracture. *Energies* **15**, 6769. https://doi.org/10.3390/en15186769 (2022).
25. Huo, D. & Benson, S. M. Experimental investigation of stress-dependency of relative permeability in rock fractures. *Transp. Porous Media* **113**, 567–590. https://doi.org/10.1007/s11242-016-0713-z (2016).
26. Watanabe, N. *et al.* New v-type relative permeability curves for two-phase flows through subsurface fractures. *Water Resour. Res.* **51**, 2807–2824. https://doi.org/10.1002/2014WR016515 (2015).
27. Cardona, A., Finkbeiner, T. & Santamarina, J. C. Natural rock fractures: From aperture to fluid flow. *Rock Mech. Rock Eng.* **54**, 5827–5844. https://doi.org/10.1007/s00603-021-02565-1 (2021).
28. Reitsma, S. & Kueper, B. H. Laboratory measurement of capillary pressure-saturation relationships in a rock fracture. *Water Resour. Res.* **30**, 865–878. https://doi.org/10.1029/93WR03451 (1994).
29. Bertels, S. P., DiCarlo, D. A. & Blunt, M. J. Measurement of aperture distribution, capillary pressure, relative permeability, and in situ saturation in a rock fracture using computed tomography scanning. *Water Resour. Res.* **37**, 649–662. https://doi.org/10.1029/2000WR900316 (2001).
30. Wang, Y., Wu, C. & Zhou, Y. Effect study of aperture distribution on the capillary pressure-saturation relation for the single fracture. *Geofluids* **2017**, 9656393. https://doi.org/10.1155/2017/9656393 (2017).
31. Sun, Z., Jang, J. & Santamarina, J. C. Time-dependent pore filling. *Water Resour. Res.* https://doi.org/10.1029/2018WR023066 (2018).
32. Cardona, A. & Santamarina, J. C. Immiscible imbibition in fractured media: A dual-porosity microfluidics study. *Int. J. Rock Mech. Min. Sci.* https://doi.org/10.1016/j.ijrmms.2023.105555 (**in press**)

33. Weerakone, W. M. S. B., Wong, R. C. K. & Mehrotra, A. K. Measurement of capillary pressure curve of DNAPL in a water-saturated sandstone fracture. *J. Geotechn. Geoenviron. Eng.* **138**, 614–624. https://doi.org/10.1061/(ASCE)GT.1943-5606.0000590 (2012).

34. Yang, Z., Neuweiler, I., Méheust, Y., Fagerlund, F. & Niemi, A. Fluid trapping during capillary displacement in fractures. *Adv. Water Resour.* **95**, 264–275. https://doi.org/10.1016/j.advwatres.2015.07.015 (2016).

35. Wang, L. & Cardenas, M. B. Connecting pressure-saturation and relative permeability models to fracture properties: The case of capillary-dominated flow of supercritical CO2 and brine. *Water Resour. Res.* **54**, 6965–6982. https://doi.org/10.1029/2018WR023526 (2018).

36. Hu, R., Zhou, C.-X., Wu, D.-S., Yang, Z. & Chen, Y.-F. Roughness control on multiphase flow in rock fractures. *Geophys. Res. Lett.* **46**, 12002–12011. https://doi.org/10.1029/2019GL084762 (2019).

37. Ye, Z., Liu, H.-H., Jiang, Q., Liu, Y. & Cheng, A. Two-phase flow properties in aperture-based fractures under normal deformation conditions: Analytical approach and numerical simulation. *J. Hydrol.* **545**, 72–87. https://doi.org/10.1016/j.jhydrol.2016.12.017 (2017).

38. da Silva, J. A., Kang, P. K., Yang, Z., Cueto-Felgueroso, L. & Juanes, R. Impact of confining stress on capillary pressure behavior during drainage through rough fractures. *Geophys. Res. Lett.* **46**, 7424–7436. https://doi.org/10.1029/2019GL082744 (2019).

39. Power, W. & Durham, W. Topography of natural and artificial fractures in granitic rocks: Implications for studies of rock friction and fluid migration. *Int. J. Rock Mech. Min. Sci.* **34**, 979–989. https://doi.org/10.1016/S1365-1609(97)80007-X (1997).

40. Candela, T. *et al.* Roughness of fault surfaces over nine decades of length scales. *J. Geophys. Res. Solid Earth* https://doi.org/10.1029/2011JB009041 (2012).

41. Briggs, S., Karney, B. W. & Sleep, B. E. Numerical modeling of the effects of roughness on flow and eddy formation in fractures. *J. Rock Mech. Geotechn. Eng.* **9**, 105–115. https://doi.org/10.1016/j.jrmge.2016.08.004 (2017).

42. Jefferys, W. H. & Berger, J. O. Ockham's Razor and Bayesian analysis. *Am. Sci.* **80**, 64–72 (1992).

43. Kang, P. K., Brown, S. & Juanes, R. Emergence of anomalous transport in stressed rough fractures. *Earth Planet. Sci. Lett.* **454**, 46–54. https://doi.org/10.1016/j.epsl.2016.08.033 (2016).

44. Jackson, R. L. & Green, I. A finite element study of elasto-plastic hemispherical contact against a rigid flat. *J. Tribol.* **127**, 343–354. https://doi.org/10.1115/1.1866166 (2005).

45. Glass, R. J., Nicholl, M. J. & Yarrington, L. A modified invasion percolation model for low-capillary number immiscible displacements in horizontal rough-walled fractures: Influence of local in-plane curvature. *Water Resour. Res.* **34**, 3215–3234. https://doi.org/10.1029/98WR02224 (1998).

46. Hughes, R. G. & Blunt, M. J. Network modeling of multiphase flow in fractures. *Adv. Water Resour.* **24**, 409–421. https://doi.org/10.1016/S0309-1708(00)00064-6 (2001).

47. Yang, Z., Niemi, A., Fagerlund, F. & Illangasekare, T. Two-phase flow in rough-walled fractures: Comparison of continuum and invasion-percolation models. *Water Resour. Res.* **49**, 993–1002. https://doi.org/10.1002/wrcr.20111 (2013).

48. Glass, R. J., Rajaram, H. & Detwiler, R. L. Immiscible displacements in rough-walled fractures: Competition between roughening by random aperture variations and smoothing by in-plane curvature. *Phys. Rev. E* **68**, 061110. https://doi.org/10.1103/PhysRevE.68.061110 (2003).

49. Joekar-Niasar, V., Doster, F., Armstrong, R., Wildenschild, D. & Celia, M. A. Trapping and hysteresis in two-phase flow in porous media: A pore-network study. *Water Resour. Res.* **49**, 4244–4256. https://doi.org/10.1002/wrcr.20313 (2013).

50. Rücker, M. *et al.* From connected pathway flow to ganglion dynamics. *Geophys. Res. Lett.* **42**, 3888–3894. https://doi.org/10.1002/2015GL064007 (2015).

51. Bear, J. & Cheng, A.H.-D. *Modeling groundwater flow and contaminant transport* Vol. 23 (Springer, 2010).

52. Luckner, L., van Genuchten, M. T. & Nielsen, D. A consistent set of parametric models for the two-phase flow of immiscible fluids in the subsurface. *Water Resour. Res.* **25**, 2187–2193. https://doi.org/10.1029/WR025i010p02187 (1989).

53. Dai, S. & Santamarina, J. C. Water retention curve for hydrate-bearing sediments. *Geophys. Res. Lett.* **40**, 5637–5641. https://doi.org/10.1002/2013GL057884 (2013).

54. Jaynes, E. T. *Probability Theory : The Logic of Science.* (Cambridge University Press, 2003).

55. Ash, R. B. *Probability and Measure Theory* 2nd edn. (Academic Press, 1999).

56. Mandelbrot, B. B., Passoja, D. E. & Paullay, A. J. Fractal character of fracture surfaces of metals. *Nature* **308**, 721–722. https://doi.org/10.1038/308721a0 (1984).

Acknowledgements

Author contributions

All authors contributed equally to conceptualization, investigation and writing. All authors reviewed the manuscript.

Competing interests

The authors declare no competing interests.

Additional information

Correspondence and requests for materials should be addressed to Q.L.

Reprints and permissions information is available at www.nature.com/reprints.

Publisher's note Springer Nature remains neutral with regard to jurisdictional claims in published maps and institutional affiliations.